

16 **1. Abstract**

17 There is increasing interest in understanding how the phase and amplitude of distinct neural oscillations
18 might interact to support dynamic communication within the brain. In particular, previous work has
19 demonstrated a coupling between the phase of low frequency oscillations and the amplitude (or power) of
20 high frequency oscillations during certain tasks, termed phase amplitude coupling (PAC). For instance,
21 during visual processing in humans, PAC has been reliably observed between ongoing alpha (8-13Hz) and
22 gamma-band (>40Hz) activity. However, the application of PAC metrics to electrophysiological data can
23 be challenging due to numerous methodological issues and lack of coherent approaches within the field.
24 Therefore, in this article we outline the various analysis steps involved in detecting PAC, using an openly
25 available MEG dataset from 16 participants performing an interactive visual task. Firstly, we localised
26 gamma and alpha-band power using the Fieldtrip toolbox, and extracted time courses from area V1,
27 defined using a multimodal parcellation scheme. These V1 responses were analysed for changes in alpha-
28 gamma PAC, using four common algorithms. Results showed an increase in gamma (40-100Hz) - alpha
29 (7-13Hz) PAC in response to the visual grating stimulus, though specific patterns of coupling were
30 somewhat dependent upon the algorithm employed. Additionally, post-hoc analyses showed that these
31 results were not driven by the presence of non-sinusoidal oscillations, and that trial length was sufficient to
32 obtain reliable PAC estimates. Finally, throughout the article, methodological issues and practical
33 guidelines for ongoing PAC research will be discussed.

35 **2. Introduction**

36 Electrophysiological brain oscillations are often separated into distinct frequency bands, ranging from low-
37 frequency delta (1-4Hz) to high-frequency gamma (<40Hz). The power and/or connectivity profiles of
38 these frequency bands have been linked with specific neuronal and cognitive functions (Buzsáki &
39 Draguhn, 2004; Palva, Palva, & Kaila, 2005). Whilst this has proven a powerful tool in neuroscientific
40 research, there is emerging evidence that oscillations from different frequency bands also display specific
41 coupling patterns – a phenomenon termed cross frequency coupling (CFC) (Hyafil, Giraud, Fontolan, &
42 Gutkin, 2015; Jensen & Colgin, 2007). One of the best studied forms of CFC is phase-amplitude coupling
43 (PAC), in which the amplitude/power of a high frequency oscillation, often gamma (>40Hz), is coupled to
44 the phase of a lower frequency oscillation (Canolty et al., 2006; Canolty & Knight, 2010). PAC has been
45 observed in multiple regions of the human brain, including the visual cortex (Voytek et al., 2010), auditory
46 cortex (Cho et al., 2015), hippocampus (Heusser, Poeppel, Ezzyat, & Davachi, 2016; Lega, Burke, Jacobs,
47 & Kahana, 2014) and prefrontal cortex (Voloh, Valiante, Everling, & Womelsdorf, 2015; Voytek et al.,
48 2015), in both electrocorticography (ECOG) and magnetoencephalography (MEG) recordings.

49
50 Within the visual system, there is strong evidence for a dynamic coupling between alpha phase (8-13Hz)
51 and gamma amplitude (>40Hz) (Bonfond & Jensen, 2015; Spaak, Bonfond, Maier, Leopold, &
52 Jensen, 2012; Voytek et al., 2010). Alpha oscillations are associated with pulses of cortical inhibition
53 every ~100ms (Jensen & Mazaheri, 2010; Klimesch, 2012), whilst supporting communication through

54 phase dynamics (Fries, 2015). In contrast, gamma oscillations emerge through local excitatory and
55 inhibitory interactions, and synchronise local patterns of cortical activity (Buzsáki & Wang, 2012; Singer
56 & Gray, 1995). In visual cortex, ongoing gamma-band activity becomes temporally segmented by distinct
57 phases of alpha-band activity (Bonfond, Kastner, & Jensen, 2017; Spaak et al., 2012), possibly via inter-
58 laminar coupling between supragranular and infragranular cortical layers (Mejias, Murray, Kennedy, &
59 Wang, 2016). Intriguingly, this coupling has been proposed to act as a mechanism for the dynamic co-
60 ordination of brain activity over multiple spatial scales, with high-frequency activity within local
61 ensembles coupled to large-scale patterns of low-frequency phase synchrony (Bonfond et al., 2017),
62 both within the visual system (Bonfond & Jensen, 2015), and more widespread neurocognitive networks
63 (Florin & Baillet, 2015). This would allow information to be routed efficiently between areas and for
64 neuronal representations to be segmented and maintained, for example during visual working memory
65 (Bonfond & Jensen, 2015; Lisman & Idiart, 1995). Atypical patterns of PAC have also been proposed to
66 underlie atypical cortical connectivity in several neurological conditions, including autism spectrum
67 disorder (Kessler, Seymour, & Rippon, 2016; Khan et al., 2013), schizophrenia (Kirihaara, Rissling,
68 Swerdlow, Braff, & Light, 2012) and Parkinson's Disease (De Hemptinne et al., 2013; Özkurt &
69 Schnitzler, 2011).

70

71 Given the developing interest in cross-frequency coupling, it is vital for the wider neuroscience and
72 electrophysiological community to understand the steps involved in its measurement and interpretation.
73 This is especially important for PAC, which is beset with methodological pitfalls, since there are many
74 competing algorithms, approaches, and currently no gold-standard set of analysis steps (Canolty & Knight,
75 2010; Jensen, Spaak, & Park, 2016). It has also been suggested that numerous incidences of reported PAC
76 may in fact be false positives, caused by suboptimal analysis practices and/or the presence of artefacts
77 within the data (Aru et al., 2015; Hyafil, 2015). For example non-sinusoidal sawtooth-like oscillations can
78 generate artificially inflated PAC values, via low-frequency phase harmonics (Cole et al., 2017; Lozano-
79 Soldevilla, ter Huurne, & Oostenveld, 2016; Vaz, Yaffe, Wittig Jr, Inati, & Zaghoul, 2017).

80

81 In this article, we outline a general approach for detecting changes in phase-amplitude coupling during
82 visual processing, using a novel MEG dataset, analysed using the Fieldtrip toolbox (Oostenveld, Fries,
83 Maris, & Schoffelen, 2010), and openly available MATLAB scripts. Four common PAC algorithms were
84 used to quantify the coupling between ongoing alpha phase (7-13Hz) and gamma amplitude/power
85 (>40Hz) whilst participants viewed a static visual grating. Given the controversy surrounding PAC
86 analysis, methodological steps were outlined in detail and justified by existing empirical research.
87 Furthermore, follow-up analyses were conducted to establish the reliability of our results and to assess
88 whether patterns of alpha-gamma PAC were driven by non-sinusoidal oscillations or insufficient data.

89

90 3. Methods

91 3.1 Participants

92 Data were collected from 16 participants (6 male, 10 female, mean age = 28.25, SD = 6.23). All
93 participants had normal or corrected to normal vision and no history of neurological or psychiatric illness.

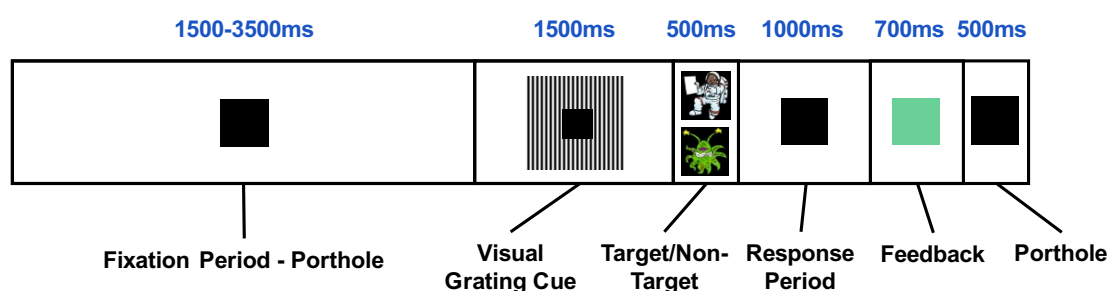
95 3.2 Experimental Procedures

96 All experimental procedures complied with the Declaration of Helsinki and were approved by the Aston
97 University, Department of Life & Health Sciences ethics committee.

99 3.3 Paradigm

100 Participants performed an engaging sensory paradigm (figure 1), designed to elicit patterns of high-
101 frequency oscillatory activity. Each trial started with a fixation period of 1500-3500ms, followed by the
102 presentation of a visual grating or auditory binaural click train cue; however only visual data will be
103 analysed in this article. The visual grating had a spatial frequency of 2 cycles/degree and was presented for
104 1500ms. Following this, participants were instructed to respond to the appearance of an alien stimulus (go)
105 or astronaut stimulus (no-go) using a response pad. The astronaut/alien stimulus was presented for 500ms
106 followed by a maximum response period of 1000ms. The accuracy of the response was conveyed through
107 audio-visual feedback, followed by a 500ms baseline period. In total, the MEG recording lasted 12-13
108 minutes and included 64 trials with visual grating stimuli. Prior to MEG acquisition, the nature of the task
109 was fully explained to participants and several practice trials were performed. Accuracy rates were above
110 95% for all participants indicating that the task was engaging and successfully understood.

111



112

113 *Figure 1:* The structure of the engaging sensory paradigm, in which participants were instructed to respond
114 after the appearance of the alien stimulus. Each trial started with a 1500-3500ms baseline period in which a
115 square black box (the “porthole”) was centrally presented. This was followed by presentation of the visual
116 grating (2 cycles/degree) around the central porthole for 1500ms. The target stimulus (alien) or non-target
117 stimulus (astronaut) was then shown within the porthole for 500ms followed by a 1000ms response period.
118 Correct or incorrect responses were conveyed to the participant through audio-visual feedback in which the
119 porthole turned green (correct) or red (incorrect) and a correct/incorrect tone was played.

120

121 **3.4 MEG Acquisition**

122 MEG data were acquired using a 306-channel Neuromag MEG scanner (Vectorview, Elekta, Finland)
123 made up of 102 triplets of two orthogonal planar gradiometers and one magnetometer. All recordings were
124 performed inside a magnetically shielded room at a sampling rate of 1000Hz. Five head position indicator
125 (HPI) coils were applied for continuous head position tracking, and visualised post-acquisition using an in-
126 house Matlab script. For MEG-MRI coregistration purposes three fiducial points, the locations of the HPI
127 coils and 300-500 points from the head surface were acquired using the integrated Polhemus Fastrak
128 digitizer.

129
130 Visual stimuli were presented on a screen located 86cm from participants (resulting in 2 cycles/degree for
131 the visual grating), and auditory feedback through MEG-compatible headphones.

132

133 **3.5 Structural MRI**

134 A structural T1 brain scan was acquired for source reconstruction using a Siemens MAGNETOM Trio 3T
135 scanner with a 32-channel head coil (TE=2.18ms, TR=2300ms, TI=1100ms, flip angle=9, 192 or 208
136 slices depending on head size, voxel-size = 0.8x0.8x0.8cm).

137

138 **3.6 MEG-MRI Coregistration and 3D Cortical Mesh Construction**

139 MEG data were co-registered with participants MRI structural scan by matching the digitised head shape
140 data with surface data from the structural scan (Jenkinson & Smith, 2001). The aligned MRI-MEG image
141 was used to create a forward model based on a single-shell description of the inner surface of the skull
142 (Nolte, 2003), using the segmentation function in SPM8 (Litvak et al., 2011). The cortical mantle was then
143 extracted to create a 3D cortical mesh, using Freesurfer v5.3 (Fischl, 2012), and registered to a standard
144 fs_LR mesh, based on the Conte69 brain (Van Essen 2012), using an interpolation algorithm from the
145 Human Connectome Project (Van Essen et al., 2012; instructions here: <https://goo.gl/3HYA3L>). Finally,
146 the mesh was downsampled to 4002 vertices per hemisphere. Due to the extensive computation time
147 involved in these procedures, all participant-specific cortical meshes are available to download in the /anat
148 directory of the Figshare repository (see later).

149

150 **3.7 Pre-processing**

151 MEG data were pre-processed using Maxfilter (temporal signal space separation, .9 correlation), which
152 suppresses external sources of noise from outside the head (Taulu & Simola, 2006).

153

154 Further pre-processing steps were performed in Matlab 2014b using the open-source Fieldtrip toolbox
155 v20161024 (Oostenveld et al., 2010; script: 1_preprocessing_elektra_frontiers_PAC.m). Firstly, for each
156 participant the entire recording was band-pass filtered between 0.5-250Hz (Butterworth filter, low-pass
157 order 4, high-pass order 3) and band-stop filtered (49.5-50.5Hz; 99.5-100.5Hz) to remove residual 50Hz
158 power-line contamination and its harmonics. Data were then epoched into segments of 4000ms (2000ms

159 pre, 2000ms post stimulus onset) and each trial was demeaned and detrended. Trials containing artefacts
160 (SQUID jumps, eye-blinks, head movement, muscle) were removed if the trial-by-channel (magnetomer)
161 variance exceeded 8×10^{-23} , resulting in an average of 63.5 trials per condition, per participant. Site-specific
162 MEG channels containing large amounts of non-physiological noise were removed from all analyses
163 (MEG channels: 0111, 0332, 2542, 0532).

164

165 **3.8 Source Analysis**

166 Source analysis was conducted using a linearly constrained minimum variance beamformer (LCMV) (Van
167 Veen, van Drongelen, Yuchtman, & Suzuki, 1997), which applies a spatial filter to the MEG data at each
168 vertex of the 3D cortical mesh, in order to maximise signal from that location whilst attenuating signals
169 elsewhere. Beamforming weights were calculated by combining the covariance matrix of the sensor data
170 with leadfield information. Due to rank reduction following data cleaning with Maxfilter, the covariance
171 matrix was kept at a rank which explained 99% of the variance. For all analyses, a common filter was used
172 across baseline and grating periods, and a regularisation parameter of lambda 5% was applied.

173

174 Due to prior interest in the gamma and alpha-bands (Hoogenboom, Schoffelen, Oostenveld, Parkes, &
175 Fries, 2006; Michalareas et al., 2016; Muthukumaraswamy, Singh, Swettenham, & Jones, 2010), the visual
176 data were band-pass filtered (Butterworth filter) between 40-60Hz (gamma) and 8-13Hz (alpha), and
177 source analysis was performed separately for each frequency band. To capture induced rather than evoked
178 visual activity, a period of 300-1500ms following stimulus onset was compared with a 1200ms baseline
179 period. The change in oscillatory power for each vertex was averaged across participants, interpolated onto
180 a 3D mesh provided by the Human Connectome Project (Van Essen, 2012), and thresholded at a value
181 which allowed the prominent patterns of power changes to be determined.

182

183 **3.9 Extracting Area V1 Time-series**

184 Trial time-courses were extracted from bilateral visual area V1, defined using a multi-modal parcellation
185 from the Human Connectome Project, which combined retinotopic mapping, T1/T2 structural MRI and
186 diffusion-weighted MRI to accurately define the boundaries between cortical areas (Glasser et al., 2016;
187 Figure 3C). The downsampled version of this atlas can be found in the parent directory of the Figshare
188 repository (see later). To obtain a single spatial filter from this region, we performed a principle
189 components analysis (PCA) on the concatenated filters from 182 vertices of bilateral V1, multiplied by the
190 sensor-level covariance matrix, and extracted the first component. The sensor-level data was then
191 multiplied by this spatial filter to obtain a V1-specific “virtual electrode”, and the change in oscillatory
192 power between grating and baseline periods was calculated from 1-100Hz, using a sliding window of
193 500ms and fixed frequency smoothing (± 8 Hz) (Hoogenboom, Schoffelen, Oostenveld, Parkes, & Fries,
194 2006). It is important to note that while we decided to use a multimodal atlas, visual area V1 virtual
195 electrode time-series could also be defined using a more standard volumetric approach, for example the
196 AAL atlas, which is included in the Fieldtrip toolbox (Oostenveld et al., 2010).

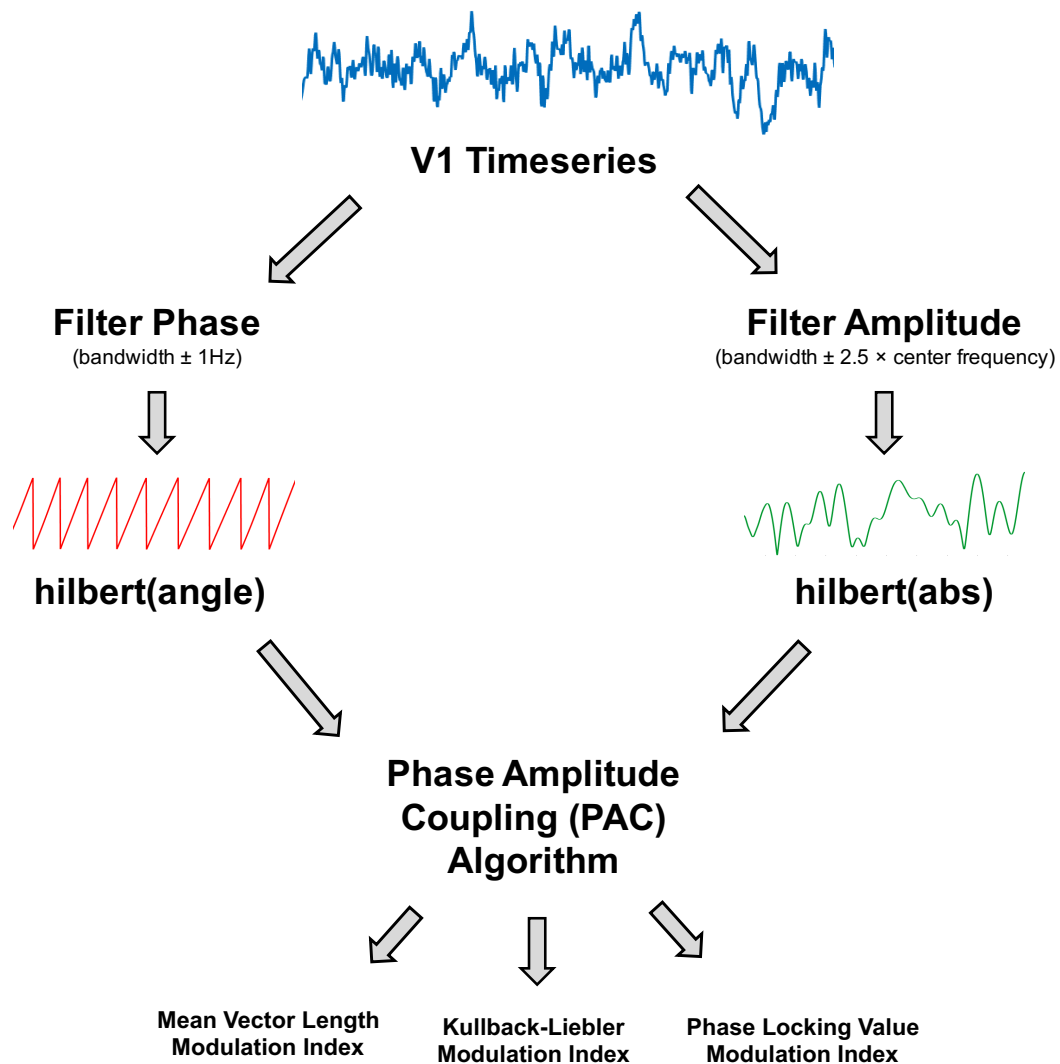
197 **3.10 Phase Amplitude Coupling (PAC) Analysis**

198 V1 time-courses were examined for changes in alpha-gamma phase amplitude coupling (PAC). The
199 general procedure is outlined in Figure 2. The first step was to obtain estimates of low frequency phase
200 (f_p) and high frequency amplitude (f_a) for each trial using a fourth order, two-pass Butterworth filter, and
201 then applying the Hilbert transform (Le Van Quyen et al., 2001). To avoid sharp edge artefacts, which can
202 result in spurious PAC (Kramer, Tort, & Kopell, 2008), the first 800ms and last 500ms of each trial was
203 discarded.

204

205 The bandwidth of the filter used to obtain f_p and f_a is a crucial parameter in calculating PAC (Aru et al.,
206 2015). The filters for extracting f_a need to be wide enough to capture the centre frequency \pm the
207 modulating f_p . So, for example, to detect PAC between $f_p = 13\text{Hz}$ and $f_a = 60\text{Hz}$, requires a f_a bandwidth
208 of at least 13Hz [47 73]. If this condition is not met, then PAC cannot be detected even if present (Dvorak
209 & Fenton, 2014). We therefore decided to use a variable bandwidth, defined as ± 2.5 times the center
210 frequency (e.g. for an amplitude of 60Hz, the bandwidth was 24Hz either side [36 84]), which has been
211 shown to improve the ability to detect PAC (Berman et al., 2012; Voloh et al., 2015). For alpha-band
212 phase (maximum 13Hz), this allowed us to calculate PAC for amplitudes above 34Hz. The bandwidth for
213 f_p was kept narrow (1Hz \pm the center frequency), in order to extract sinusoidal waveforms. Furthermore,
214 each trial was visually inspected to confirm that the f_p filtered oscillations were sinusoidal in nature.

215



216

217 *Figure 2:* Illustration of the phase amplitude coupling (PAC) analysis procedure. The V1 time-series were
218 filtered to obtain estimates of phase and amplitude, using a narrow ($\pm 1\text{Hz}$) bandwidth for the phase and a
219 variable bandwidth (± 2.5 times the centre frequency) for the amplitude. Phase and amplitude information
220 were obtained via the Hilbert transform. The coupling between phase and amplitude was then quantified
221 using Mean Vector Length, Kullback-Leiber or Phase Locking Value algorithms to produce a Modulation
222 Index value.

223

224 Next, the coupling between f_p and f_a was quantified using four common PAC approaches¹: the Mean-
225 Vector Length modulation index, originally described in Canolty et al., (2006); the Mean-Vector Length
226 modulation index described in Özkurt & Schnitzler (2011); the phase-locking value modulation index
227 described in Cohen (2008); and the Kullback-Lieber modulation index described in Tort, Komorowski,

¹ Due to inconsistent naming practices, we refer to the quantitative value of PAC as the modulation index (MI) across all four approaches.

228 Eichenbaum, & Kopell (2010a). These approaches were selected due to their popularity in the MEG/EEG
229 PAC literature (e.g. Bonnefond & Jensen, 2015; Cho et al., 2015; Khan et al., 2013; Mathewson et al.,
230 2011), and to demonstrate the diversity of PAC results based on the algorithm selected.

231

232 The mean vector length modulation index (MVL-MI-Canolty) approach estimates PAC by combining
233 phase (ϕ) and amplitude information to create a complex-valued signal: $f_a e^{i(\phi f_p)}$ (Canolty et al., 2006), in
234 which each vector corresponds to a certain time-point (N). If the resulting probability distribution function
235 is non-uniform, this suggests a coupling between f_p and f_a , which can be quantified by taking the length of
236 the average vector.

237

$$238 \quad MI = \left| \sum_{n=1}^N f_a(n) e^{i(\phi f_p(n))} \right|$$

239

240 However, MI values from the MVL-MI-Canolty algorithm have been shown to partly reflect the power of
241 f_a oscillations, rather than their coupling (Canolty & Knight, 2010). Therefore, as an alternative to
242 surrogate data, we applied a MVL-MI algorithm from Özkurt & Schnitzler (2011), which includes a
243 normalisation factor corresponding to the power of f_a . Özkurt & Schnitzler (2011) suggest that their
244 algorithm is more resilient to measurement noise, and is therefore highly relevant for MEG data, which has
245 an inherently lower signal-to-noise ratio compared with invasive electrophysiological recordings
246 (Goldenholz et al., 2009).

247

$$248 \quad MI = \frac{1}{\sqrt{N}} \frac{\left| \sum_{n=1}^N f_a(n) e^{i(\phi f_p(n))} \right|}{\sqrt{\sum_{n=1}^N f_a(n)^2}}$$

249

250 The PLV-MI-Cohen approach assumes that if PAC is present, the envelope of f_a should oscillate at the
251 frequency corresponding to f_p . The phase of f_a envelope can be obtained by applying the Hilbert transform
252 (angle): ϕf_a . The coupling between the low-frequency ϕf_p phase values and the phase of the amplitude
253 envelope, ϕf_a , can be quantified by calculating a phase locking value (PLV), in much the same way as
254 determining phase synchronisation between electrophysiological signals.

255

$$256 \quad MI = \left| \frac{1}{n} \sum_{N=1}^n e^{i(\phi f_p(N) - \phi f_a(N))} \right|$$

257

258 Finally, the KI-MI-Tort approach estimates PAC by quantifying the amount of deviation in amplitude-
259 phase distributions. This involves breaking f_p into 18 bins, and calculating the mean amplitude within each
260 phase bin, normalised by the average value across all bins. The modulation index is calculated by
261 comparing the amplitude-phase distribution (P) against the null hypothesis of a uniformly amplitude-phase
262 distribution (Q).

263

264

$$MI = \frac{D(P, Q)}{\log(N_{bins})}$$

265

266 Mathematically, this is computed using the Kullbeck-Leiber distance (D), related to Shannon's entropy.

267

$$D(P, Q) = \sum_{i_{bin}=1}^N P(i_{bin}) \cdot \log\left(\frac{P(i_{bin})}{Q(i_{bin})}\right)$$

268

269 Using these four approaches (MVL-MI-Canolty; MVL-MI-Özkurt; KL-MI-Tort; PLV-MI-Cohen) we
270 calculated PAC between phases 7-13Hz (in 1 Hz steps) and amplitudes 34-100Hz (in 2Hz steps), for the
271 time-period 300-1500ms following grating presentation and a 1200ms baseline period. PAC values were
272 calculated separately for each trial and then averaged to obtain a single MI value per amplitude and phase.
273 This was repeated using surrogate data, created by shuffling trial and phase-carrying information (200
274 surrogates), to normalise MI values. On a PC with 32GB of RAM, and Intel(R) Core™ i7-4790 processor,
275 the computation time for these procedures was 4.5 hours.

276

277 To assess changes in the strength of PAC between the grating and baseline periods, the comodulograms
278 were compared using non-parametric cluster-based statistics, which have been shown to adequately control
279 the type-I error rate for electrophysiological data (Maris & Oostenveld, 2007). First, an uncorrected
280 dependent-samples t-test was performed (grating versus baseline), and all MI values exceeding a 5%
281 significance threshold were grouped into clusters. The maximum t-value within each cluster was carried
282 forward. Next, a null distribution was obtained by randomising the condition label (grating/baseline) 1000
283 times and calculating the largest cluster-level t-value for each permutation. The maximum t-value within
284 each original cluster was then compared against this null distribution, with values exceeding a threshold of
285 $p < .05$ deemed significant.

286

287 **3.11 Sinusoidal Oscillations**

288 One major issue in cross-frequency coupling analysis is the presence of non-sinusoidal sawtooth-like
289 oscillations (Cole et al., 2017; Jensen et al., 2016), which can result in spurious estimates of PAC (Lozano-
290 Soldevilla et al., 2016). This property of oscillations can be quantified by calculating the time taken from
291 trough to peak (rise-time), peak to trough (decay-time), and the ratio between these values (Cole &
292 Voytek, 2017; Dvorak & Fenton, 2014). We therefore calculated this ratio for the visual V1 data from 7-
293 13Hz, to check for differences in non-sinusoidal oscillations between grating and baseline periods.

294

295 **3.12 Simulated PAC Analysis**

296 To investigate the validity of the four PAC approaches, we constructed 1.2 seconds of simulated data with
297 known alpha-gamma PAC ($f_p = 10\text{Hz}$; $f_a = 50\text{-}70\text{Hz}$; code adapted from Kramer et al., (2008) and Özkurt
298 & Schnitzler (2011)) and added a random level of noise (signal-to-noise ratio $> -11.5\text{Db}$). Comodulograms

299 were produced using the four PAC algorithms on 64 trials of simulated data. Using the same code, we also
300 investigated how the four algorithms were affected by trial length (0.1-10s in 0.1 second steps).

301

302 **3.13 Analysis Code & Data Sharing**

303 MEG data are available to download online at Figshare

304 (<https://doi.org/10.6084/m9.figshare.c.3819106.v1>), along with participant-specific 3D cortical meshes.

305 Access to the raw structural MRI data will be granted upon reasonable request and ethical approval from

306 Aston University Life & Health Sciences ethics committee. MATLAB code used for all analyses has been

307 made available in the supplementary materials and online (https://github.com/neurofractal/sensory_PAC),

308 including the four PAC algorithms, which can be applied to electrophysiological data arranged in the

309 standard Fieldtrip format (Oostenveld et al., 2010). Successful use of the scripts requires the user to have at

310 least a basic understanding of MATLAB, signal processing, and the methodological complexities

311 surrounding PAC. We therefore direct the reader to a number of excellent reviews and empirical papers

312 (Aru et al., 2015; Canolty et al., 2006; Canolty & Knight, 2010; Hyafil et al., 2015; Jensen & Colgin,

313 2007).

314

315 **4. Results**

316 **4.1 Source Localisation**

317 In order to establish patterns of oscillatory power changes following presentation of the visual grating,

318 gamma-band (40-60Hz) and alpha-band power (8-13Hz) were localised for a 300-1500ms period post-

319 stimulus presentation. Results for the gamma-band (figure 3A), show an increase in oscillatory power

320 which localises to the ventral occipital cortex (Hoogenboom et al., 2006). Results for the alpha band

321 (figure 3B) showed a general decrease in power, located primarily in occipital areas, but extending into

322 temporal and parietal regions. The more widespread spatial pattern could reflect on-going upstream

323 processes triggered by the appearance of the grating, for example anticipation of the upcoming target

324 (Stenner, Bauer, Haggard, Heinze, & Dolan, 2014).

325

326 **4.2 Visual Area V1 Power Changes**

327 Time courses from area V1 were extracted (figure 3C), and the change in oscillatory power between

328 grating and baseline periods from 1-100Hz was calculated (figure 3D). Whilst results show individual

329 variability in peak frequencies and the strength of oscillatory power, on average, activity within visual area

330 V1 displays a reduction in alpha/beta power (8-20Hz), and an increase in gamma power (40-70Hz). The

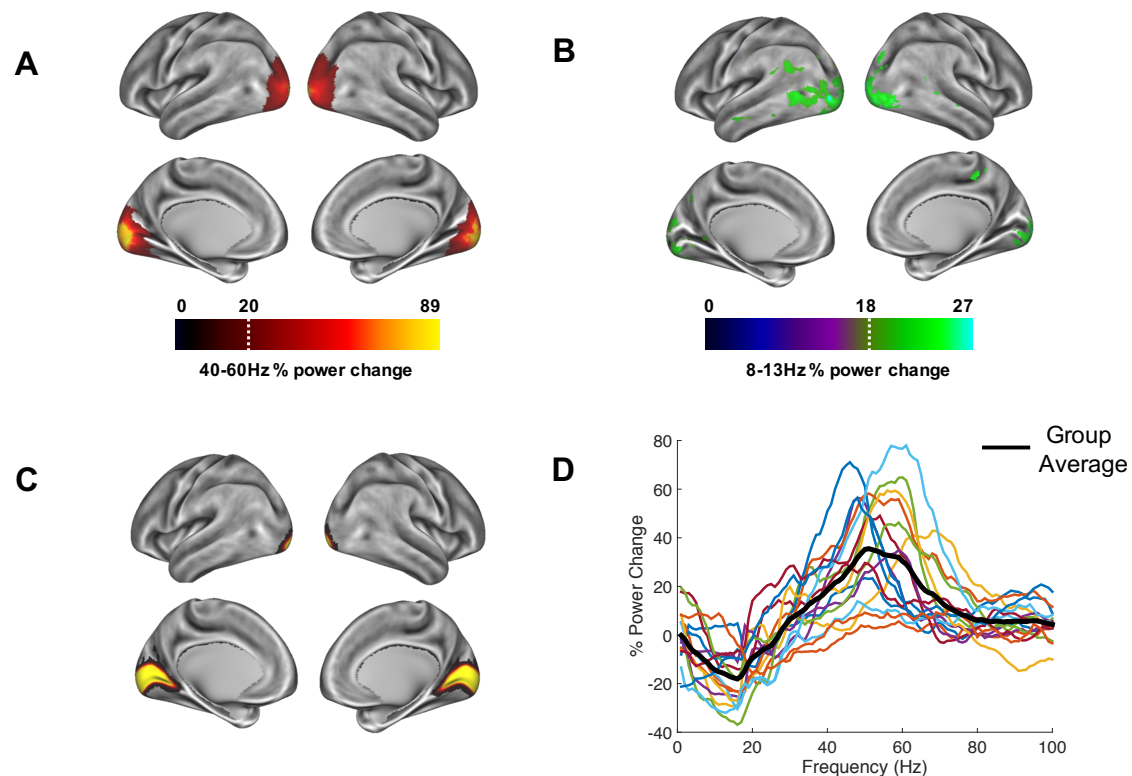
331 MEG data, therefore display well-established patterns of alpha and gamma-band event-related

332 synchronisation and desynchronisation within visual area V1 (Bonnefond & Jensen, 2015; Hoogenboom et

333 al., 2006; Michalareas et al., 2016), which is a crucial first step in calculating reliable estimates of PAC

334 (Aru et al., 2015).

335



336

337 *Figure 3:* Whole-brain oscillatory power changes following the presentation of the visual grating are
338 marked by **(A)** increases in the gamma-band (40-60Hz) and **(B)** decreases in the alpha-band (8-13Hz),
339 localised primarily in the ventral occipital cortex (script: 2_get_source_power.m). Power maps were
340 thresholded at a value which allowed prominent patterns of power changes to be determined, indicated by
341 the white dotted line. Time-courses were extracted from bilateral visual area V1 (script:
342 3_get_VE_frontiers_PAC.m), defined using the atlas region shown in **(C)** from the HCP-MMP 1.0
343 parcellation (Glasser et al., 2016). **(D)** These V1 responses showed reductions in alpha/beta power and
344 increases in gamma-band (40-70Hz) power (script: 4_calc_pow_change.m).

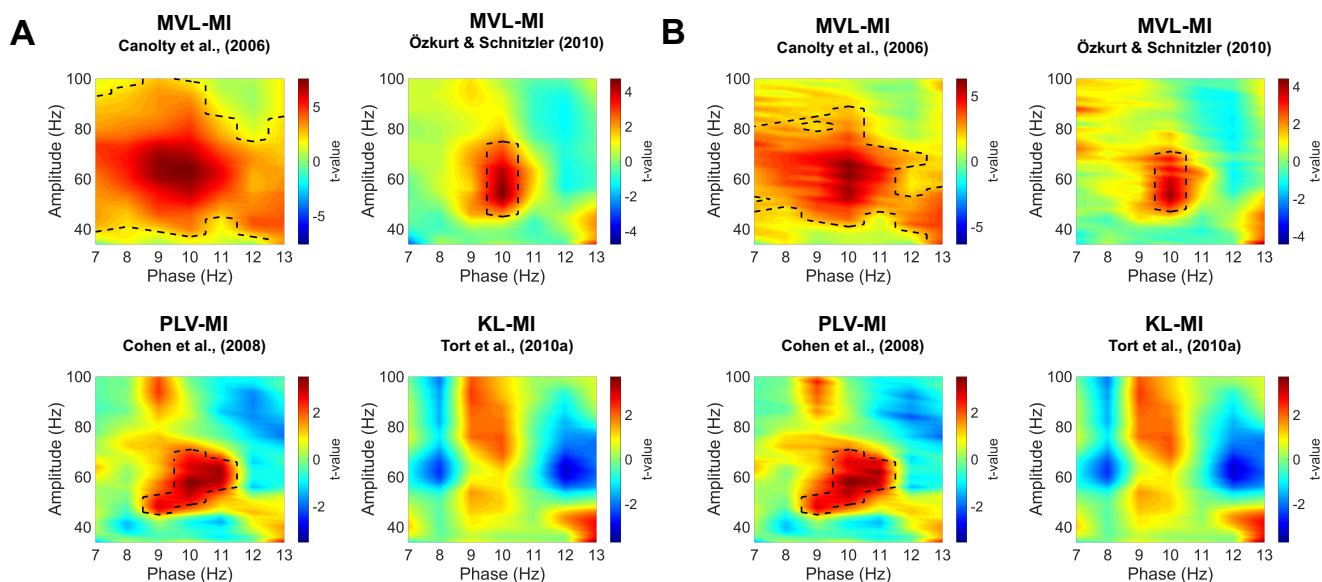
345

346 4.3 Alpha-Gamma PAC

347 Visual area V1 responses were next examined for changes in alpha-gamma PAC. Specifically, we set out
348 to test whether the coupling between alpha-band phase and gamma-band amplitude was altered during
349 presentation of the visual grating. Phase-amplitude comodulograms were produced between a range of
350 phase frequencies (7-13Hz) and amplitude frequencies (34-100Hz), using the four algorithms described in
351 Methods: MVL-MI-Canolty; MVL-MI-Özkurt; PLV-MI-Cohen and KL-MI-Tort. Grating and baseline
352 comodulograms were compared using cluster-based non-parametric statistics (Maris & Oostenveld, 2007).

353

354 Results are shown in Figure 4A. Using the MVL-MI-Canolty algorithm, there was a significant increase in
 355 alpha-gamma PAC over a large proportion of the comodulogram, between 40-100Hz and 7-13Hz, with a
 356 peak at 50-70Hz amplitude and 9-10Hz phase. This large area of significantly increased PAC is likely to
 357 reflect, in part, power increases in the gamma-band (Canolty et al., 2006). The alternative MVL-MI-
 358 Özkurt algorithm, which normalises MI values by the high-frequency oscillatory power, displayed a
 359 smaller area of significant coupling, with increased PAC between an amplitude of 50-70Hz and phase of
 360 10Hz. There was also a similar cluster of significantly increased PAC between 9-11Hz and 50-70Hz using
 361 the PLV-MI-Cohen approach. The KL-MI-Tort results showed clusters of increased PAC between
 362 amplitudes of 50-100Hz and phases of 9-10Hz, but decreased PAC between amplitudes of 60-90Hz and
 363 phases of 12-13Hz. However, none of these clusters passed a significance threshold of $p < 0.05$ (two-tailed).
 364 Similar results were obtained after normalising MI values with surrogate data (Figure 4B).



365
 366 *Figure 4:* Phase-amplitude comodulograms produced by statistically comparing modulation index (MI)
 367 values from 300ms-1500ms post-grating onset to a 1200ms baseline period, using four separate approaches
 368 (script: 5_visual_PAC_four_methods.m). Comodulograms for (A) raw MI values and (B) MI values
 369 normalised by surrogate data are shown separately. The black dotted line represents significantly different
 370 phase-amplitude coupling frequencies ($p < .05$; for details of non-parametric cluster-based statistics see
 371 Methods).

372

373 4.4 Non-Sinusoidal Oscillations

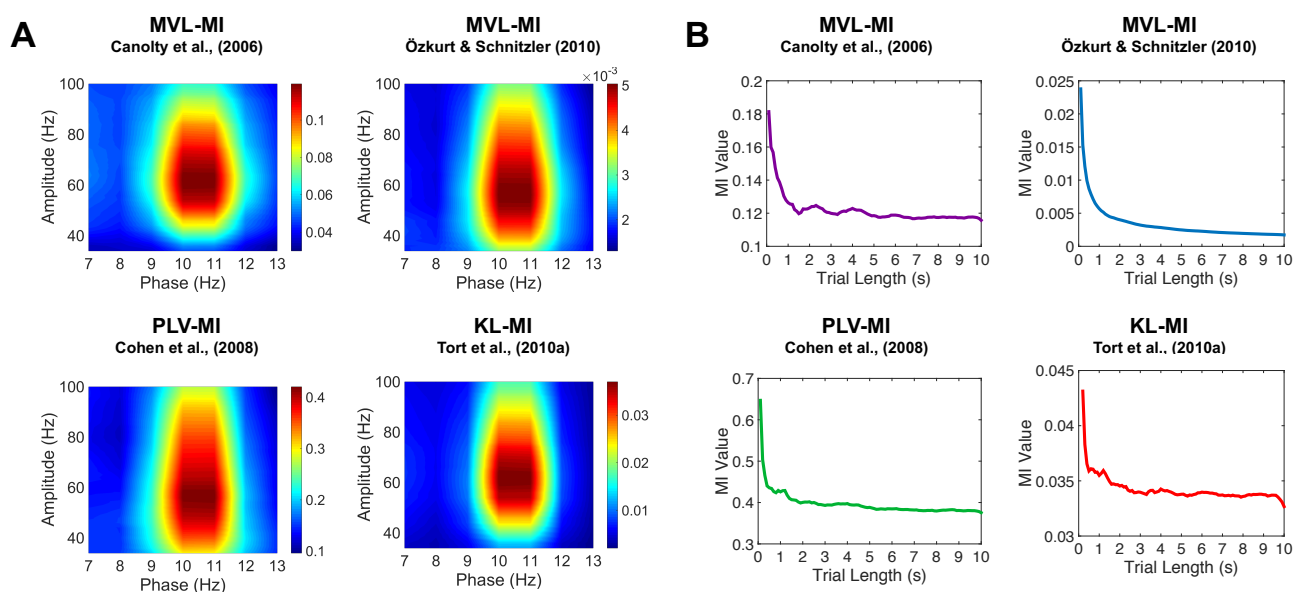
374 To determine whether our alpha-gamma PAC results were driven by differences in the sinusoidal
 375 properties of oscillations between baseline and grating periods, the ratio between oscillatory rise-time and
 376 decay-time was calculated (6_check_non_sinusoidal.m). For the alpha phase frequencies (7-13Hz), there
 377 was no difference in this ratio (all frequencies $p > .05$), suggesting that our results are unlikely to be caused

378 by increased non-sinusoidal sawtooth-like properties of alpha oscillations during stimulus period compared
379 to baseline.

380

381 4.5 Simulated PAC

382 To further validate our PAC results, we generated simulated data with known alpha-gamma coupling (10-
383 11Hz phase, 50-70Hz amplitude). Using the same MATLAB code as for the MEG data, we were able to
384 successfully detect this alpha-gamma PAC using the MVL-MI-Canolty, MVL-MI-Özkurt, PLV-MI-Cohen
385 and KL-MI-Tort algorithms (Figure 5A). By varying the trial length of the simulated data, we found that
386 PAC values were affected by trial length, with data segments under 1 second producing artificially inflated
387 PAC (Figure 5B).



388 *Figure 5: Results of the simulated PAC analysis. (A)* Phase-amplitude comodulograms produced using the
389 MVL-MI-Canolty, MVL-MI-Özkurt, PLV-MI-Cohen and KL-MI-Tort algorithms were able to
390 successfully detect the simulated coupling between 10Hz phase and 50-70Hz amplitude. **(B)** The coupling
391 between 10Hz phase and 60Hz amplitude was calculated as a function of simulated data trial length. For
392 trial data under 1 second, all four algorithms produced artificially inflated PAC (script:
393 7_simulated_PAC_analysis.m).

394

395 5. Discussion

396 This article has outlined various steps involved in the detection and validation of phase amplitude coupling
397 (PAC) in a visual MEG dataset (data shared at: <https://doi.org/10.6084/m9.figshare.c.3819106.v1>),
398 utilising the open-source Fieldtrip toolbox (Oostenveld et al., 2010) and customised Matlab scripts (all
399 scripts shared at: https://github.com/neurofractal/sensory_PAC). We first confirmed that presentation of
400 the visual grating was accompanied by decreases in alpha power (8-13Hz) and increases in gamma power
401 (>40Hz) within visual area V1. Although this may seem redundant given the wealth of evidence for alpha
402 and gamma oscillations in visual processing (Bonnefond & Jensen, 2015; Hoogenboom et al., 2006;
403 Michalareas et al., 2016), it is crucial to establish clear increases/decreases in the power spectrum at two
404 distinct frequencies as a first step in MEG-PAC analysis (Aru et al., 2015; Hyafil et al., 2015). Using four
405 PAC algorithms, we showed that visual responses obtained from area V1 displayed a general increase in
406 alpha-gamma PAC as expected (Bonnefond & Jensen, 2015; Spaak et al., 2012; Voytek et al., 2010).
407 However, it is important to note that specific patterns of coupling depended on the algorithm selected. The
408 MVL-MI-Canolty algorithm showed large increases in PAC during the grating period, covering almost the
409 entire alpha & gamma frequency ranges, most likely as a result of MI values being biased by increases in
410 high-frequency power following presentation of the visual grating (Canolty et al., 2006). This approach is
411 therefore less suitable for detecting PAC between separate periods of data and/or trials. The MVL-MI-
412 Özkurt algorithm, which normalises the MI value by high amplitude power, along with the PLV-MI-Cohen
413 algorithm produced a much more constrained pattern of significant alpha-gamma PAC, with peaks
414 between 9-11Hz phase and 50-70Hz amplitude. Whilst the KL-MI-Tort approach also showed a general
415 increase in alpha-gamma PAC around 9-11Hz, none of the phase-amplitude clusters reached significance.
416 This may be due to the relatively short number of trials used in the experiment, the low signal-to-noise
417 ratio of MEG recordings (Goldenholz et al., 2009), variations in the peak alpha and gamma oscillatory
418 frequencies (Muthukumaraswamy, Edden, Jones, Swettenham, & Singh, 2009), combined with the fact
419 that the KL-MI-Tort approach is relatively conservative (van Driel, Cox, & Cohen, 2015). More generally,
420 it is important to emphasise that all four PAC metrics are highly sensitive to a range of factors (Aru et al.,
421 2015; Dvorak & Fenton, 2014), which are often hard to control (Berman et al., 2012), resulting in both
422 type I and type II statistical errors.

423
424 One such issue is the presence of non-sinusoidal sawtooth-like oscillations in electrophysiological data,
425 which can result in spurious PAC (Lozano-Soldevilla et al., 2016), especially when phase is obtained with
426 wide band-pass filters. By computing the ratio between rise-time and decay-time of alpha oscillations
427 within area V1, we showed that non-sinusoidal oscillations did not differ between baseline and grating
428 periods, and are unlikely to account for our results. Another issue in trial-based PAC analysis is data
429 length, with some previous reports suggesting that 10 seconds or more is required for detecting theta-
430 gamma coupling (Aru et al., 2015; Dvorak & Fenton, 2014). However, using simulated alpha-gamma PAC
431 we determined that 1 second of data was sufficient to obtain stable estimates. We encourage the reader to
432 run similar follow-up analyses after finding significant PAC to check for spurious coupling caused by, for

433 example, non-sinusoidal oscillations (Jensen et al., 2016; Lozano-Soldevilla et al., 2016) and/or
434 insufficiently long trials (Dvorak & Fenton, 2014).

435

436 **5.1 Practical Considerations for PAC analysis**

437 Cross-frequency coupling is gaining significant interest within the electrophysiological community (Aru et
438 al., 2015; Canolty & Knight, 2010; Dvorak & Fenton, 2014; Hyafil et al., 2015), and therefore it is
439 important for researchers to consider the methodological pitfalls and caveats which commonly arise during
440 PAC analysis. Firstly, due to the presence of edge artefacts at the start and end of time-series created by
441 bandpass filtering, which can result in artefactual PAC (Kramer et al., 2008), sufficient padding should be
442 included around trials. Concatenating data from separate trials to create longer data segments results in
443 similar edge artefacts (Kramer et al., 2008), and should be avoided. Secondly, if the bandwidth of the filter
444 used to extract the amplitude does not contain the side-bands of the modulating phase frequency, PAC
445 cannot be detected even if present (Dvorak & Fenton, 2014). The use of a variable band-pass filter which
446 scales with amplitude, can alleviate this issue and improve the sensitivity of detecting PAC (Berman et al.,
447 2012; Voloh et al., 2015). Thirdly, periods which contain non-stationary periods should be avoided. This
448 includes sensory evoked potentials which induce correlations between frequency bands via phase reset
449 (Sauseng et al., 2007), and can be misinterpreted as PAC (Aru et al., 2015). For this reason, we did not
450 analyse the first 300ms following visual grating presentation, due to the presence of visual evoked
451 potentials (Di Russo, Martínez, Sereno, Pitzalis, & Hillyard, 2002). Fourth, given that PAC algorithms
452 produce values ranging from 0 to 1, data are commonly not normally distributed, and therefore the use of
453 non-parametric statistics is paramount. Whilst surrogate data are often employed (Aru et al., 2015; Tort et
454 al., 2010a), this may not be possible where data are organised into short trials and temporal correlations
455 between surrogate and true time-series are high (Dvorak & Fenton, 2014). Therefore, to assess changes in
456 PAC, using a baseline period or contrasting between conditions, combined with non-parametric statistics
457 may prove to be a useful alternative for sensory neurocognitive research.

458

459 **5.2 Limitations**

460 This study has compared four PAC algorithms (Canolty et al., 2006; Cohen, 2008; Özkurt & Schnitzler,
461 2011; Tort et al., 2010a), which are among the most commonly used approaches in sensory EEG/MEG
462 research (Bonnefond & Jensen, 2015; Cho et al., 2015; Khan et al., 2013; Mathewson et al., 2011).
463 However these only comprise a small subset of the available algorithms designed to quantify PAC
464 (Canolty & Knight, 2010; Hyafil et al., 2015). There have also been advances in measuring transient
465 changes in PAC (Dvorak & Fenton, 2014), directed PAC (Jiang, Bahramisharif, van Gerven, & Jensen,
466 2015) and algorithms designed for spontaneous neural activity (Florin & Baillet, 2015; Weaver et al.,
467 2016). A more comprehensive evaluation of algorithms and their application to real-world
468 electrophysiological data is beyond the scope of this article, but would nevertheless benefit the field of
469 cross-frequency coupling. Secondly, in order to detect alpha-gamma PAC within visual area V1, we used a
470 broad filter bandwidth, defined as ± 2.5 times the amplitude centre-frequency. Consequently, the alpha-

471 gamma comodulograms will be unable to differentiate between adjacent gamma sub-bands, which have
472 been proposed to fulfil differing neurocognitive roles (Bosman, Lansink, & Pennartz, 2014; Buzsáki &
473 Wang, 2012), and patterns of PAC (Vaz et al., 2017). However, for the visual MEG data presented here,
474 there was only an increase in gamma power within one band (40-70Hz), and therefore the smearing of
475 adjacent sub-bands is unlikely. Finally, we have focussed on PAC within the visual cortex, which is known
476 to display highly sinusoidal alpha oscillations (Tort et al., 2010b). However, there are many examples of
477 non-sinusoidal brain oscillations caused by physiological neuronal spiking patterns (Fontanini & Katz,
478 2005), including hippocampal theta (4-8Hz) and sensorimotor mu (9-11Hz) rhythms (Lozano-Soldevilla et
479 al., 2016; Scheffer-Teixeira & Tort, 2016), which are indicative of behaviour and disease states (Cole &
480 Voytek, 2017). Therefore, whilst non-sinusoidal oscillations generate spurious PAC, this does not mean
481 that these oscillations are uninteresting, but simply that common PAC algorithms, such as the ones
482 employed in this article, are ill-suited for these scenarios. Where non-sinusoidal oscillations are present,
483 PAC analysis could proceed by correcting for non-uniform phase distributions (e.g van Driel, Cox, &
484 Cohen, 2015) in order to disentangle nested oscillations from neural spiking (Vaz et al., 2017).

485

486 **5.3 Conclusion**

487 In conclusion, we have outlined the key analysis steps for detecting changes in alpha-gamma PAC during
488 sensory processing, using an example visual MEG dataset. While alpha-gamma PAC was shown to
489 increase, the specific patterns of alpha-gamma coupling depended upon the specific algorithm employed.
490 Follow-up analyses showed that these results were not driven by non-sinusoidal oscillations or insufficient
491 data. In future, we hope that a variety of PAC algorithms will be implemented alongside existing open-
492 source MEG toolboxes (Gramfort et al., 2014; Oostenveld et al., 2010; Tadel, Baillet, Mosher, Pantazis, &
493 Leahy, 2011), with detailed guidance and advice, so that PAC can form a natural analysis step in
494 electrophysiological research.

495

496 **6. Author Contributions**

497 RS, KK & GR co-designed the study and wrote the manuscript. RS collected the data, carried out the
498 analysis and organised the data and code for sharing.

499

500 **7. Conflict of Interests Statement**

501 The authors wish to declare the research was conducted in the absence of any commercial or financial
502 relationships that could be construed as a potential conflict of interest.

503

504 **8. Acknowledgments**

505 We wish to thank: the volunteers who gave their time to participate in this study; Jan-Mathijs Schoffelen
506 for providing MATLAB code; Gerard Gooding-Williams and Shu Yau for help with MRI data acquisition;
507 Diandra Brkic for helpful comments on the manuscript and the Wellcome and Dr Hadwen Trusts for
508 supporting MEG scanning costs.

509

510 9. References

- 511 Aru, J., Aru, J., Priesemann, V., Wibral, M., Lana, L., Pipa, G., ... Vicente, R. (2015). Untangling cross-
512 frequency coupling in neuroscience. *Current Opinion in Neurobiology*, 31, 51–61.
- 513 Berman, J. I., McDaniel, J., Liu, S., Cornew, L., Gaetz, W., Roberts, T. P., & Edgar, J. (2012). Variable
514 bandwidth filtering for improved sensitivity of cross-frequency coupling metrics. *Brain
515 Connectivity*, 2(3), 155–163.
- 516 Bonnefond, M., & Jensen, O. (2015). Gamma Activity Coupled to Alpha Phase as a Mechanism for Top-
517 Down Controlled Gating. *PLOS ONE*, 10(6), e0128667.
- 518 Bonnefond, M., Kastner, S., & Jensen, O. (2017). Communication between Brain Areas Based on Nested
519 Oscillations. *ENeuro*, 4(2), ENEURO–0153.
- 520 Bosman, C. A., Lansink, C. S., & Pennartz, C. (2014). Functions of gamma-band synchronization in
521 cognition: from single circuits to functional diversity across cortical and subcortical systems.
522 *European Journal of Neuroscience*, 39(11), 1982– 1999.
- 523 Buzsáki, G., & Draguhn, A. (2004). Neuronal oscillations in cortical networks. *Science*, 304(5679), 1926–
524 1929.
- 525 Buzsáki, G., & Wang, X.-J. (2012). Mechanisms of gamma oscillations. *Annual Review of Neuroscience*,
526 35, 203.
- 527 Canolty, R. T., Edwards, E., Dalal, S. S., Soltani, M., Nagarajan, S. S., Kirsch, H. E., ... Knight, R. T.
528 (2006). High gamma power is phase-locked to theta oscillations in human neocortex. *Science*,
529 313(5793), 1626–1628.
- 530 Canolty, R. T., & Knight, R. T. (2010). The functional role of cross-frequency coupling. *Trends in
531 Cognitive Sciences*, 14(11), 506–515.
- 532 Cho, R. Y., Walker, C. P., Polizzotto, N. R., Wozny, T. A., Fissell, C., Chen, C.-M. A., & Lewis, D. A.
533 (2015). Development of sensory gamma oscillations and cross-frequency coupling from childhood
534 to early adulthood. *Cerebral Cortex*, 25(6), 1509– 1518.
- 535 Cohen, M. X. (2008). Assessing transient cross-frequency coupling in EEG data. *Journal of
536 Neuroscience Methods*, 168(2), 494–499.
- 537 Cole, S. R., van der Meij, R., Peterson, E. J., de Hemptinne, C., Starr, P. A., & Voytek, B. (2017).
538 Nonsinusoidal beta oscillations reflect cortical pathophysiology in Parkinson's disease. *Journal of
539 Neuroscience*, 37(18), 4830–4840.
- 540 Cole, S. R., & Voytek, B. (2017). Brain Oscillations and the Importance of Waveform Shape. *Trends in
541 Cognitive Sciences*, 21(2), 137–149.
- 542 De Hemptinne, C., Ryapolova-Webb, E. S., Air, E. L., Garcia, P. A., Miller, K. J., Ojemann, J. G., ...
543 Starr, P. A. (2013). Exaggerated phase–amplitude coupling in the primary motor cortex in
544 Parkinson disease. *Proceedings of the National Academy of Sciences*, 110(12), 4780–4785.
- 545 Di Russo, F., Martínez, A., Sereno, M. I., Pitzalis, S., & Hillyard, S. A. (2002). Cortical sources of the
546 early components of the visual evoked potential. *Human Brain Mapping*, 15(2), 95–111.

- 547 Dvorak, D., & Fenton, A. A. (2014). Toward a proper estimation of phase–amplitude coupling in neural
548 oscillations. *Journal of Neuroscience Methods*, 225, 42–56.
- 549 Essen, V., C, D., Glasser, M. F., Dierker, D. L., Harwell, J., & Coalson, T. (2012). Parcellations and
550 Hemispheric Asymmetries of Human Cerebral Cortex Analyzed on Surface-Based Atlases.
551 *Cerebral Cortex*, 22(10), 2241–2262.
- 552 Fischl, B. (2012). FreeSurfer. *Neuroimage*, 62(2), 774–781.
- 553 Florin, E., & Baillet, S. (2015). The brain’s resting-state activity is shaped by synchronized cross-
554 frequency coupling of neural oscillations. *NeuroImage*, 111, 26–35.
- 555 Fontanini, A., & Katz, D. B. (2005). 7 to 12 Hz activity in rat gustatory cortex reflects disengagement from
556 a fluid self-administration task. *Journal of Neurophysiology*, 93(5), 2832–2840.
- 557 Fries, P. (2015). Rhythms for cognition: communication through coherence. *Neuron*, 88(1), 220–235.
- 558 Glasser, M. F., Coalson, T. S., Robinson, E. C., Hacker, C. D., Harwell, J., Yacoub, E., ... Van Essen, D.
559 C. (2016). A multi-modal parcellation of human cerebral cortex. *Nature*, 536(7615), 171–178.
- 560 Goldenholz, D. M., Ahlfors, S. P., Hämäläinen, M. S., Sharon, D., Ishitobi, M., Vaina, L. M., &
561 Stufflebeam, S. M. (2009). Mapping the signal-to-noise-ratios of cortical sources in
562 magnetoencephalography and electroencephalography. *Human Brain Mapping*, 30(4),
563 1077–1086.
- 564 Gramfort, A., Luessi, M., Larson, E., Engemann, D. A., Strohmeier, D., Brodbeck, C., ... Hämäläinen, M.
565 S. (2014). MNE software for processing MEG and EEG data. *Neuroimage*, 86, 446–460.
- 566 Heusser, A. C., Poeppel, D., Ezzyat, Y., & Davachi, L. (2016). Episodic sequence memory is supported by
567 a theta-gamma phase code. *Nature Neuroscience*, 19(10), 1374–1380.
- 568 Hoogenboom, N., Schoffelen, J.-M., Oostenveld, R., Parkes, L. M., & Fries, P. (2006). Localizing human
569 visual gamma-band activity in frequency, time and space. *Neuroimage*, 29(3), 764–773.
- 570 Hyafil, A. (2015). Misidentifications of specific forms of cross-frequency coupling: three warnings.
571 *Frontiers in Neuroscience*, 9.
- 572 Hyafil, A., Giraud, A.-L., Fontolan, L., & Gutkin, B. (2015). Neural Cross-Frequency Coupling:
573 Connecting Architectures, Mechanisms, and Functions. *Trends in Neurosciences*, 38(11), 725–
574 740.
- 575 Jenkinson, M., & Smith, S. (2001). A global optimisation method for robust affine registration of brain
576 images. *Medical Image Analysis*, 5(2), 143–156.
- 577 Jensen, O., & Colgin, L. L. (2007). Cross-frequency coupling between neuronal oscillations. *Trends in*
578 *Cognitive Sciences*, 11(7), 267–269.
- 579 Jensen, O., & Mazaheri, A. (2010). Shaping functional architecture by oscillatory alpha activity: gating by
580 inhibition. *Frontiers in Human Neuroscience*, 4, 186.
- 581 Jensen, O., Spaak, E., & Park, H. (2016). Discriminating valid from spurious indices of phase-amplitude
582 coupling. *eNeuro*, 3(6), ENEURO–0334.
- 583 Jiang, H., Bahramisharif, A., van Gerven, M. A., & Jensen, O. (2015). Measuring directionality between
584 neuronal oscillations of different frequencies. *Neuroimage*, 118, 359–367.

- 585 Kessler, K., Seymour, R. A., & Rippon, G. (2016). Brain oscillations and connectivity in autism spectrum
586 disorders (ASD): new approaches to methodology, measurement and modelling. *Neuroscience &*
587 *Biobehavioral Reviews*, 71, 601–620.
- 588 Khan, S., Gramfort, A., Shetty, N. R., Kitzbichler, M. G., Ganesan, S., Moran, J. M., ... Kenet, T. (2013).
589 Local and long-range functional connectivity is reduced in concert in autism spectrum disorders.
590 *Proceedings of the National Academy of Sciences*, 110(8), 3107–3112.
- 591 Kirihara, K., Rissling, A. J., Swerdlow, N. R., Braff, D. L., & Light, G. A. (2012). Hierarchical
592 Organization of Gamma and Theta Oscillatory Dynamics in Schizophrenia. *Biological Psychiatry*,
593 71(10), 873–880.
- 594 Klimesch, W. (2012). Alpha-band oscillations, attention, and controlled access to stored information.
595 *Trends in Cognitive Sciences*, 16(12), 606–617.
- 596 Kramer, M. A., Tort, A. B., & Kopell, N. J. (2008). Sharp edge artifacts and spurious coupling in EEG
597 frequency comodulation measures. *Journal of Neuroscience Methods*, 170(2), 352–357.
- 598 Le Van Quyen, M., Foucher, J., Lachaux, J.-P., Rodriguez, E., Lutz, A., Martinerie, J., & Varela, F. J.
599 (2001). Comparison of Hilbert transform and wavelet methods for the analysis of neuronal
600 synchrony. *Journal of Neuroscience Methods*, 111(2), 83–98.
- 601 Lega, B., Burke, J., Jacobs, J., & Kahana, M. J. (2014). Slow-theta-to-gamma phase– amplitude coupling
602 in human hippocampus supports the formation of new episodic memories. *Cerebral Cortex*, 26(1),
603 268-278.
- 604 Lisman, J. E., & Idiart, M. A. (1995). Storage of 7 plus/minus 2 short-term memories in oscillatory
605 subcycles. *Science*, 267(5203), 1512.
- 606 Litvak, V., Mattout, J., Kiebel, S., Phillips, C., Henson, R., Kilner, J., ... others. (2011). EEG and MEG
607 data analysis in SPM8. *Computational Intelligence and Neuroscience*, 2011.
- 608 Lozano-Soldevilla, D., ter Huurne, N., & Oostenveld, R. (2016). Neuronal oscillations with non-sinusoidal
609 morphology produce spurious phase-to-amplitude coupling and directionality. *Frontiers in*
610 *Computational Neuroscience*, 10, 87-100.
- 611 Maris, E., & Oostenveld, R. (2007). Nonparametric statistical testing of EEG- and MEG-data.
612 *Journal of Neuroscience Methods*, 164(1), 177–190.
- 613 Mathewson, K. E., Lleras, A., Beck, D. M., Fabiani, M., Ro, T., & Gratton, G. (2011). Pulsed out of
614 awareness: EEG alpha oscillations represent a pulsed-inhibition of ongoing cortical processing.
615 *Frontiers in Psychology*, 2, 99.
- 616 Mejias, J. F., Murray, J. D., Kennedy, H., & Wang, X.-J. (2016). Feedforward and feedback frequency-
617 dependent interactions in a large-scale laminar network of the primate cortex. *Science Advances*,
618 2(11).
- 619 Michalareas, G., Vezoli, J., van Pelt, S., Schoffelen, J.-M., Kennedy, H., & Fries, P. (2016). Alpha-Beta
620 and Gamma Rhythms Subserve Feedback and Feedforward Influences among Human Visual
621 Cortical Areas. *Neuron*, 89(2), 384-397.

- 622 Muthukumaraswamy, S. D., Edden, R. A., Jones, D. K., Swettenham, J. B., & Singh, K. D. (2009). Resting
623 GABA concentration predicts peak gamma frequency and fMRI amplitude in response to visual
624 stimulation in humans. *Proceedings of the National Academy of Sciences*, 106(20), 8356–8361.
- 625 Muthukumaraswamy, S. D., Singh, K. D., Swettenham, J. B., & Jones, D. K. (2010). Visual gamma
626 oscillations and evoked responses: variability, repeatability and structural MRI correlates.
627 *Neuroimage*, 49(4), 3349–3357.
- 628 Nolte, G. (2003). The magnetic lead field theorem in the quasi-static approximation and its use for
629 magnetoencephalography forward calculation in realistic volume conductors. *Physics in Medicine
630 and Biology*, 48(22), 3637–3652.
- 631 Oostenveld, R., Fries, P., Maris, E., & Schoffelen, J.-M. (2010). FieldTrip: open source software for
632 advanced analysis of MEG, EEG, and invasive electrophysiological data. *Computational
633 Intelligence and Neuroscience*, 2011.
- 634 Özkurt, T. E., & Schnitzler, A. (2011). A critical note on the definition of phase–amplitude cross-
635 frequency coupling. *Journal of Neuroscience Methods*, 201(2), 438–443.
- 636 Palva, J. M., Palva, S., & Kaila, K. (2005). Phase synchrony among neuronal oscillations in the human
637 cortex. *Journal of Neuroscience*, 25(15), 3962–3972.
- 638 Sauseng, P., Klimesch, W., Gruber, W. R., Hanslmayr, S., Freunberger, R., & Doppelmayr, M. (2007).
639 Are event-related potential components generated by phase resetting of brain oscillations? A
640 critical discussion. *Neuroscience*, 146(4), 1435–1444.
- 641 Scheffer-Teixeira, R., & Tort, A. B. (2016). On cross-frequency phase-phase coupling between theta and
642 gamma oscillations in the hippocampus. *eLife*, 5, e20515.
- 643 Singer, W., & Gray, C. M. (1995). Visual feature integration and the temporal correlation hypothesis.
644 *Annual Review of Neuroscience*, 18(1), 555–586.
- 645 Spaak, E., Bonnefond, M., Maier, A., Leopold, D. A., & Jensen, O. (2012). Layer-specific entrainment of
646 gamma-band neural activity by the alpha rhythm in monkey visual cortex. *Current Biology*,
647 22(24), 2313–2318.
- 648 Stenner, M.-P., Bauer, M., Haggard, P., Heinze, H.-J., & Dolan, R. (2014). Enhanced alpha-oscillations in
649 visual cortex during anticipation of self-generated visual stimulation. *Journal of Cognitive
650 Neuroscience*. 26(11), 2540–2551.
- 651 Tadel, F., Baillet, S., Mosher, J. C., Pantazis, D., & Leahy, R. M. (2011). Brainstorm: a user- friendly
652 application for MEG/EEG analysis. *Computational Intelligence and Neuroscience*, 2011, 8.
- 653 Taulu, S., & Simola, J. (2006). Spatiotemporal signal space separation method for rejecting nearby
654 interference in MEG measurements. *Physics in Medicine and Biology*, 51(7), 1759.
- 655 Tort, A. B., Komorowski, R., Eichenbaum, H., & Kopell, N. (2010a). Measuring Phase-Amplitude
656 Coupling Between Neuronal Oscillations of Different Frequencies. *Journal of Neurophysiology*,
657 104(2), 1195–1210.

- 658 Tort, A. B., Fontanini, A., Kramer, M. A., Jones-Lush, L. M., Kopell, N. J., & Katz, D. B. (2010b).
659 Cortical networks produce three distinct 7–12 Hz rhythms during single sensory responses in the
660 awake rat. *Journal of Neuroscience*, 30(12), 4315–4324.
- 661 van Driel, J., Cox, R., & Cohen, M. X. (2015). Phase-clustering bias in phase–amplitude cross-frequency
662 coupling and its removal. *Journal of Neuroscience Methods*, 254, 60–72.
- 663 Van Essen (2012). Cortical cartography and Caret software. *NeuroImage*, 62(2), 757–764.
- 664 Van Essen, D. C., Ugurbil, K., Auerbach, E., Barch, D., Behrens, T. E. J., Bucholz, R., ... others. (2012).
665 The Human Connectome Project: a data acquisition perspective. *Neuroimage*, 62(4), 2222–2231.
- 666 Van Veen, B. D., van Drongelen, W., Yuchtman, M., & Suzuki, A. (1997). Localization of brain electrical
667 activity via linearly constrained minimum variance spatial filtering. *IEEE Transactions on*
668 *Biomedical Engineering*, 44(9), 867–880.
- 669 Vaz, A. P., Yaffe, R. B., Wittig Jr, J. H., Inati, S. K., & Zaghloul, K. A. (2017). Dual origins of measured
670 phase-amplitude coupling reveal distinct neural mechanisms underlying episodic memory in the
671 human cortex. *NeuroImage*, 148, 148–159.
- 672 Voloh, B., Valiante, T. A., Everling, S., & Womelsdorf, T. (2015). Theta–gamma coordination between
673 anterior cingulate and prefrontal cortex indexes correct attention shifts. *Proceedings of the*
674 *National Academy of Sciences*, 112(27), 8457–8462.
- 675 Voytek, B., Canolty, R. T., Shestyuk, A., Crone, N., Parvizi, J., & Knight, R. T. (2010). Shifts in Gamma
676 Phase–Amplitude Coupling Frequency from Theta to Alpha Over Posterior Cortex During Visual
677 Tasks. *Frontiers in Human Neuroscience*, 4.
- 678 Voytek, B., Kayser, A. S., Badre, D., Fegen, D., Chang, E. F., Crone, N. E., ... D’esposito, M. (2015).
679 Oscillatory dynamics coordinating human frontal networks in support of goal maintenance. *Nature*
680 *Neuroscience*, 18(9), 1318–1324.
- 681 Weaver, K. E., Wander, J. D., Ko, A. L., Casimo, K., Grabowski, T. J., Ojemann, J. G., & Darvas, F.
682 (2016). Directional patterns of cross frequency phase and amplitude coupling within the resting
683 state mimic patterns of fMRI functional connectivity. *NeuroImage*, 128, 238–251.
- 684